

# Variational Percolation Bounds for *Cellular Membrane Occlusion*

Cesar Mello<sup>1,\*</sup>

Fernando Medina da Cunha, MD<sup>2</sup>

<sup>1</sup>Cosmo Physics Organization, São Paulo, Brazil

<sup>2</sup>Centro de Oncologia Campinas, São Paulo, Brazil

`*cesar.mello@cosmophys.org`

## Abstract

Malignant membranes cluster nutrient transporters within glycan rich domains, sustaining metabolism through redundant intake routes. A theoretical framework links interfacial chemistry to transport suppression and energetic or redox collapse. The model unites a screened Poisson–Nernst–Planck electrodiffusion problem, an interfacial potential of mean force, and a reduced energetic redox module connecting flux to ATP/NADPH balance. From this structure, capacitary spectral bounds relate total flux to the inverse principal eigenvalue,

$$J_{\text{tot}} \leq C e^{-\beta \chi_{\text{eff}}} \mathcal{P}(\theta).$$

Two near orthogonal levers geometry and field strength govern a linear suppression regime below a percolation-type knee, beyond which conductance collapses. A composite intake index,

$$\Xi = w_G J_{\text{GLUT}} + w_A J_{\text{LAT/ASCT}} + w_L J_{\text{MCT}},$$

dictates energetic trajectories: once below a maintenance threshold, ATP and NADPH fall jointly and redox imbalance drives irreversible commitment. Normal membranes, with fewer transport mouths and weaker fields, remain above this threshold, defining a natural selectivity window. The framework demonstrates existence, regularity, and spectral monotonicity for the self-adjoint PNP operator, establishing a geometric–spectral transition that links molecular parameters such as branching and sulfonation to measurable macroscopic outcomes with predictive precision.

# Introduction

Solid tumors exhibit clustered nutrient transporters (GLUT1/3, LAT1/ASCT2, MCT1/4) embedded in glycan-rich microdomains [2, 12, 43]. Inspired by this organization, a purely theoretical, membrane-centric two-stage *lockdown* is formulated. In *Stage 1*, a branched sulfonated PEG scaffold (Cap–PEG–SO<sub>3</sub>) anchored by DSPE–PEG or chol–PEG imposes multichannel occlusion at transporter vestibules; in *Stage 2*, an optional prodrug layer releases payloads under tumor-specific triggers (pH, GSH, protease) [1, 17, 18]. The framework aims to map controllable interfacial chemistry onto transport and energetic/redox behavior in malignant versus non-malignant membranes.

Despite extensive work on metabolic redundancy, no quantitative scheme links interfacial architecture and sulfonation to global transport suppression and energetic failure while remaining falsifiable. Classical single-route inhibition fails under redundant intake; a unified membrane-level theory is needed to describe *multichannel* occlusion, identify the onset of conductance collapse, and define selectivity as operation below a percolation-type knee with moderated fields [3, 7].

The framework couples three layers: (i) a screened **Poisson–Nernst–Planck (PNP)** electrodiffusion problem on heterogeneous membranes with mixed boundaries, formulated in weak form under explicit regularity and screening hypotheses; (ii) an interfacial potential of mean force combining steric, electrostatic, hydration, dispersion, and multivalency terms; (iii) a reduced energetic–redox network mapping flux suppression onto ATP/NADPH balance and metabolic stability [4–6]. Together, they connect tunable chemical knobs (branching, grafting, sulfonation) to spectral conductance and redox outcomes through variational inequalities.

Two lightly orthogonal variables—geometric coverage  $\theta$  and interfacial field  $\chi_{\text{eff}}$ —govern the capacitary–spectral law

$$J_{\text{tot}} \leq C e^{-\beta \chi_{\text{eff}}} P(\theta),$$

with a percolation knee at  $\theta = \eta_c$ . Variational–spectral arguments describe how occlusion and field amplification raise the principal eigenvalue and reduce conductance. Selectivity follows from remaining below  $\eta_c$  in normal contexts, while malignant membranes exceed it. The theory yields falsifiable slopes linking molecular design to measurable observables (fluxes, ATP, NADPH, ECAR, caspases) without invoking experimental claims. The next subsection, *Controlled Orthogonality: Geometry vs. Interfacial Field*, formalizes why  $\theta$  and  $\chi_{\text{eff}}$  act as quasi-independent levers defining a predictable and safe design space.

# Theoretical Foundations

## Scope and Modeling Layers

A membrane–centric mechanism is formalized in three coupled layers: (i) an *electro-diffusive* boundary layer describing metabolite approach to transporter vestibules under screened fields; (ii) an *interfacial interaction* layer combining steric, electrostatic, hydrogen-bonding, dispersion, and hydration/depletion forces between the CAP scaffold and malignant microdomains; (iii) a *bioenergetic/network* layer where suppressed transport translates into ATP/NADPH decline and contraction of feasible flux states. The objective is a closed physics–chemistry map from molecular design variables to macroscopic flux bounds and dynamical outcomes [4, 5, 12].

## Geometry, Notation, and Assumptions

A membrane patch  $\Omega \subset \mathbb{R}^2$  hosts clustered glycan–transporter microdomains. Extracellular mouths of  $\mathcal{T} = \{\text{GLUT1/3, LAT1, ASCT2, MCT1/4}\}$  are modeled as absorbing windows  $\{\Gamma_j\}_{j=1}^N$  at centers  $\{x_j\}$ . CAP-occluded mouths are replaced by Dirichlet obstacles  $\{\Gamma_j^{\text{cap}}\}$  with effective radius  $R_{\text{eff}}$ . Mouth centers follow a clustered Poisson process of intensity  $\rho$  and cluster radius  $r_c$ , with parameters taken in physiological ranges unless noted [12, 43].

## Electro-diffusive Layer: Poisson–Nernst–Planck with Screening

For each species  $k$  (glucose, leucine, glutamine, lactate, protons), concentrations  $c_k(x, t)$  and potential  $\phi(x, t)$  satisfy

$$\partial_t c_k = \nabla \cdot \left( D_k \nabla c_k + \mu_k z_k c_k \nabla \phi \right), \quad (1)$$

$$-\nabla \cdot (\varepsilon \nabla \phi) = \sum_k z_k c_k - \rho_f, \quad (2)$$

with  $D_k$  diffusivity,  $\mu_k$  mobility,  $z_k$  valence,  $\varepsilon$  permittivity, and  $\rho_f$  fixed charge. Absorbing mouths impose flux on  $\Gamma_{\text{abs}}$ , CAP-occluded mouths enforce  $c_k=0$  and  $\phi=\psi_s$  on  $\Gamma_j^{\text{cap}}$ , and no-flux Neumann conditions hold on  $\Gamma_N$  [4–6].

**Functional setting and well-posedness.** Let  $\partial\Omega = \Gamma_{\text{abs}} \cup \Gamma_{\text{cap}} \cup \Gamma_N$  be a mixed boundary decomposition with  $\Omega$  bounded and  $C^{1,\alpha}$ . Under Debye–Hückel screening ( $|\phi|/\phi_T \ll 1$ ) and the Einstein relation  $\mu_k = D_k/(k_B T)$ , the linearized steady operator on  $H_{\Gamma_D}^1(\Omega)$  (with  $\Gamma_D = \Gamma_{\text{abs}} \cup \Gamma_{\text{cap}}$ ) is symmetric, coercive, and has compact resolvent, yielding a unique weak solution (steady) and an analytic semigroup (transient). This ensures that fluxes and access factors below are well defined within the mixed-boundary PNP framework.

**Scaling.** With  $L \sim 10\text{--}100 \text{ nm}$ ,  $\phi_T = k_B T / e$ , and nondimensional variables  $\tilde{x} = x/L$ ,  $\tilde{\phi} = \phi/\phi_T$ :

$$\delta_D = \lambda_D/L, \quad \chi_k = z_k \psi_s / \phi_T, \quad \text{Pe}_k = \frac{\|\mu_k z_k c_k \nabla \phi\| L}{\|D_k \nabla c_k\|}.$$

Screening is effective for  $\delta_D \lesssim 1$ ; strong anionic gating corresponds to  $\chi_k \gg 1$  [4].

**Boundary fluxes and linearized screening.** The normal flux for species  $k$  is  $J_k^n = (-D_k \nabla c_k - \mu_k z_k c_k \nabla \phi) \cdot n$ . On  $\Gamma_{\text{abs}}$  the (active) absorbing/uptake condition is imposed through  $J_k^n$ , on  $\Gamma_{\text{cap}}$  the constraints  $c_k = 0$  and  $\phi = \psi_s$  are enforced, and on  $\Gamma_N$  the no-flux condition  $J_k^n = 0$  holds. In the Debye–Hückel regime, linearizing (2) about  $(c_{k,\infty}, 0)$  yields the screened Poisson operator

$$-\varepsilon \Delta \phi + \varepsilon \kappa_D^2 \phi = \sum_k z_k (c_k - c_{k,\infty}), \quad \kappa_D = \lambda_D^{-1},$$

so that  $\phi$  decays on the Debye scale and couples weakly to far-field concentrations when  $\delta_D \lesssim 1$ .

**Weak formulation (linearized steady state).** Let  $V = H_{\Gamma_D}^1(\Omega)$  with  $\Gamma_D = \Gamma_{\text{abs}} \cup \Gamma_{\text{cap}}$ . For fixed  $\phi$ , the drift–diffusion operator admits the bilinear form

$$a_k(u, v) = \int_{\Omega} D_k \nabla u \cdot \nabla v dV + \int_{\Omega} \mu_k z_k \bar{c}_k \nabla \phi \cdot \nabla v dV,$$

with  $\bar{c}_k$  a positive reference profile. Coercivity of the symmetric part and compact embedding imply existence/uniqueness by Lax–Milgram/Fredholm; maximum principles control  $c_k \geq 0$  under absorbing Dirichlet/flux conditions.

**Narrow-access asymptotics and capacity.** When  $\Gamma_{\text{abs}}$  consists of small windows, the total steady flux scales with the boundary capacity,

$$J_k \sim \kappa_k^0 \text{Cap}(\Gamma_{\text{abs}}) c_{k,\infty} e^{-\beta \chi_k},$$

recovering the factorization used below: steric occlusion shrinks the effective accessible set (geometry, via  $\theta$ ), while screening and surface potential modulate entrance through a Boltzmann factor (field, via  $\chi_{\text{eff}}$ ). This matches the spectral picture  $J_{\text{tot}} \asymp \lambda_1^{-1}$  and underlies the linear–tunable regime away from the percolation knee.

# Screened electro-diffusion near occluded pores

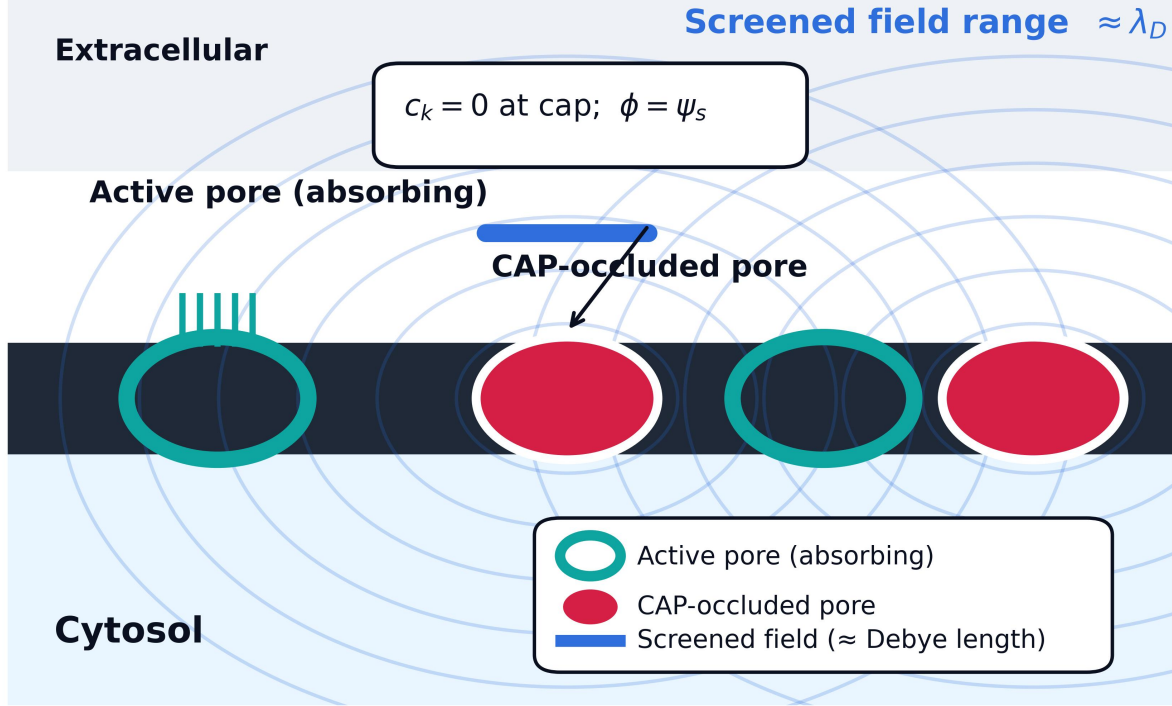


Figure 1: **Screened electro-diffusion near occluded pores.** A membrane band with alternating absorbing mouths and CAP-occluded mouths ( $c_k=0$ ,  $\phi=\psi_s$ ). The interfacial field decays over  $\lambda_D$ .

Far-field transport is set by screened PNP, while near-field access is shaped by absorbing versus occluded mouths. Within the halo of an occluded pore, approach is modulated by a potential of mean force. The resulting access factor  $\Pi_k = \exp[-\beta U_k]$ , combined with geometric coverage  $\theta$ , yields

$$J_k \approx \kappa_k^0 (1 - \theta) \Pi_k A_{\text{act}} c_{k,\infty},$$

with  $\kappa_k^0$  intrinsic access coefficient and  $A_{\text{act}}$  active absorbing area. Steric geometry ( $\theta$ ) acts broadly, charge ( $\psi_s, \lambda_D$ ) selectively [4, 7, 25].

## Interfacial Interaction Manifold

Upon tumor-gated activation, CAP experiences a composite potential  $U(r, \Omega)$  including: steric exclusion by PEG brushes; screened electrostatics from sulfonates ( $\psi_0$ ); hydrogen bonding and dispersion; hydration/depletion restructuring; and multivalency reducing  $k_{\text{off}}$ . These align with bioconjugation thermodynamics and glycan-targeting chemistries [7, 23, 25].

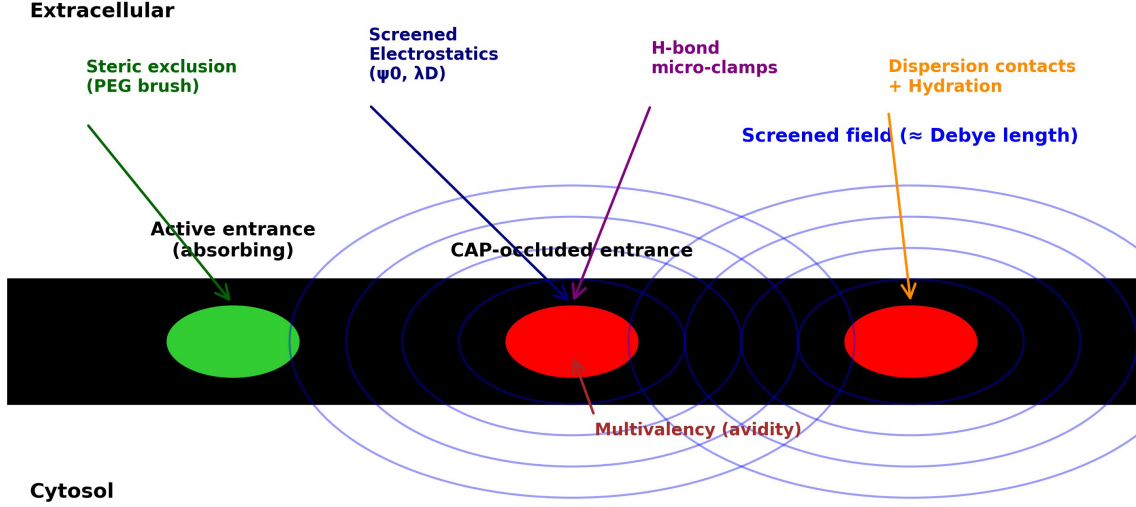


Figure 2: **Interfacial interaction manifold at a glycan–transporter cluster.** A branched PEG–SO<sub>3</sub><sup>−</sup> cap generates a composite potential-of-mean-force, stabilizing residence and narrowing access.

Two orthogonal levers emerge: geometry (coverage  $\theta$  via brush height/density) and field strength  $\chi_{\text{eff}} \propto |\psi_0|$  (via sulfonation/ionic strength). Near an entrance,

$$U_k = U_{\text{steric}} + U_{\text{el}} + U_{\text{HB}} + U_{\text{disp}} + U_{\text{hydr}} - n_{\text{val}}\Delta G_{\text{avid}}, \quad \Pi_k = e^{-\beta U_k},$$

so that

$$\kappa_k^{\text{eff}} = \kappa_k^0(1 - \theta)\Pi_k, \quad J_k \approx \kappa_k^{\text{eff}} A_{\text{act}} c_{k,\infty}.$$

This approximate orthogonality mirrors classical handles in surface engineering [7, 8, 25].

## Chemistry→Boundary Map

Brush height scales as

$$h_{\text{brush}} \sim aN_{\text{seg}}(\sigma_{\text{PEG}}a^2)^{1/3}g(N_{\text{br}}), \quad R_{\text{eff}} = R_0 + h_{\text{brush}} + \alpha_{\text{solv}}I^{-1/2}.$$

Sulfonation and pH set charge and potential,

$$\sigma_s = -\frac{eN_{\text{SO}_3}\alpha_{\text{diss}}(\text{pH})}{A}, \quad \psi_0 = \psi_s + \sigma_s/C_S, \quad \psi_s = 2\phi_T \text{asinh}\left(\frac{\sigma_s}{\sqrt{8\varepsilon k_B T c_\infty}}\right).$$

Hence  $\theta$  (geometry) and  $\psi_0$  (field) offer near-orthogonal control [7, 8, 25].

## Variational and Spectral Bounds

The PNP free-energy functional

$$\mathcal{F}[\{c_k\}, \phi] = \sum_k \int_{\Omega} \left( D_k |\nabla \sqrt{c_k}|^2 + z_k c_k \phi \right) dV + \frac{\varepsilon}{2} \int_{\Omega} |\nabla \phi|^2 dV$$

minimized under mixed boundaries yields the capacitary–variational inequality

$$J_{\text{tot}} \leq C(\{D_k\}, \Omega) e^{-\beta \chi_{\text{eff}}} \mathcal{P}(\theta).$$

For the linearized operator  $L_{\chi} = -\nabla \cdot (D \nabla) + \sigma(\chi_{\text{eff}})$  on  $H_{\Gamma_D}^1(\Omega)$ , let  $\lambda_1(\theta, \chi_{\text{eff}})$  be the principal Dirichlet eigenvalue. By domain monotonicity (increasing Dirichlet set as  $\theta \uparrow$ ) and screening ( $\sigma$  increasing with  $\chi_{\text{eff}}$ ),  $\lambda_1$  increases with  $\theta$  and  $\chi_{\text{eff}}$ ; consequently,

$$J_{\text{tot}} \asymp \frac{\text{Cap}(\Gamma_{\text{abs}})}{\lambda_1(\theta, \chi_{\text{eff}})} \lesssim C e^{-\beta \chi_{\text{eff}}} \mathcal{P}(\theta),$$

so that the effective spectral conductance  $1/\lambda_1$  shrinks with occlusion and interfacial field, in agreement with the variational law [4–6].

## Parallel with Percolation

The geometric term scales as

$$\mathcal{P}(\theta) \sim (1 - \eta_c) \left( \frac{1 - \theta}{1 - \eta_c} \right)^t, \quad t \simeq 1.3,$$

matching 2D conductivity exponents. Together,

$$J_k \sim J_k^0 (1 - \theta) e^{-\beta \chi_{\text{eff}}} \left( \frac{1 - \theta}{1 - \eta_c} \right)^{tH(\theta - \eta_c)},$$

with  $H$  the Heaviside step [4, 5].

## Bioenergetic–Redox Coupling

Let  $A(t), P(t)$  denote ATP and NADPH. A reduced model,

$$\dot{A} = y_{\text{gly}} J_{\text{GLUT}} + y_{\text{ox}} J_{\text{TCA}} - k_{\text{ATP}} \frac{A}{K_A + A}, \quad (3)$$

$$\dot{P} = y_{\text{PPP}} J_{\text{GLUT}} - k_{\text{scav}} \frac{R_{\text{ROS}}}{K_P + P}, \quad (4)$$

receives fluxes bounded by the variational law. Collapse occurs when  $(A, P)$  cross a separatrix defined by simultaneous throttling of intake and lactate handling [30–32].

## Constraint-Based Network and Identifiability

Transport caps shrink the feasible polytope  $Sv = 0$  via upper bounds  $\bar{v}_{\text{uptake},k}(J_k)$ . Shadow prices reveal emergent bottlenecks (notably lactate export). Sobol indices rank  $R_{\text{eff}}$  and  $\psi_0$  for identifiability, tying observables to chemical levers [26, 42].

## Design–Space Implications

The mechanism addresses malignant membranes with clustered, redundant nutrient mouths. Orthogonal tuning of  $\theta$  and  $\chi_{\text{eff}}$  affords quasi-linear control up to  $\eta_c$ , with abrupt collapse beyond. A theoretical selectivity window arises by operating below  $\eta_c$  and moderating  $\chi_{\text{eff}}$  in normal contexts [12, 29, 43].

## Cap–Prodrug Integration: A Two-Stage Apoptosis Switch

An extension couples starvation with gated sabotage. Stage 1: occlusion fraction  $f(t)$  follows

$$\dot{f} = k_{\text{on}}[\text{CAP}](1-f) - k_{\text{off}}f, \quad f^* = \frac{k_{\text{on}}[\text{CAP}]}{k_{\text{on}}[\text{CAP}] + k_{\text{off}}}.$$

Stage 2: payload activation  $g(t)$ ,

$$\dot{g} = k_{\text{rel}}(pH, [\text{GSH}], [\text{MMP}]) f(t)(1-g), \quad \Phi_{\text{tox}}(t) = \int_0^t \gamma f(\tau)g(\tau) d\tau.$$

Coupling to reserves,

$$\dot{A} = y_{\text{gly}}(1-f)J_{\text{GLUT}} + y_{\text{aa}}(1-f)J_{\text{LAT/ASCT}} - \alpha_A A, \quad (5)$$

$$\dot{P} = y_{\text{PPP}}(1-f)J_{\text{GLUT}} - \alpha_P P - \beta \Phi_{\text{tox}}(t), \quad (6)$$

drives irreversibility once  $(A, P)$  cross  $\Sigma = \{A < A_{\text{crit}}, P < P_{\text{crit}}\}$ . A Lyapunov functional

$$\mathcal{L}[f, g, A, P] = \frac{1}{2}(A^2 + P^2) + \lambda_1 f^2 + \lambda_2 g^2$$

decreases monotonically under joint engagement, producing hysteresis [17, 18, 21].

**Safety window.** Normal contexts require

$$J_{\text{GLUT}}^{\text{basal}}(1-f) \geq \eta_{\text{safe}} J_{\text{GLUT}}^{\text{basal}}, \quad \Phi_{\text{tox}}^{\text{normal}}(t) \leq \phi_{\text{safe}},$$

with  $f < \eta_c$  and subthreshold  $g(t)$  [30, 32].

Table 1: **Stage 1 ligand–epitope interaction: illustrative design targets used in modeling (not experimental measurements).**

Parameter	Symbol	Malignant	Non-malignant	$\Delta$ (Malig.–Non-malig.)
$K_D$		1–5 nM	>500 nM	$\lesssim -495$ nM
$k_{\text{on}}$		$1.0 \times 10^6 \text{ M}^{-1}\text{s}^{-1}$	$< 5 \times 10^4 \text{ M}^{-1}\text{s}^{-1}$	$> 9.5 \times 10^5 \text{ M}^{-1}\text{s}^{-1}$
$k_{\text{off}}$		$< 5 \times 10^{-4} \text{ s}^{-1}$	$> 2.5 \times 10^{-2} \text{ s}^{-1}$	$< -2.45 \times 10^{-2} \text{ s}^{-1}$
$\tau_{\text{res}}$		> 30 min	< 40 s	> 29.3 min
$N_{\text{ep}}$		$(2–5) \times 10^5$	$< 5 \times 10^3$	$\gtrsim (1.95–4.95) \times 10^5$
$K_D^{\text{app}}$		< 1 nM	> 200 nM	< -199 nM

The last column reports a directional contrast

$$\Delta(X) := X_{\text{Malignant}} - X_{\text{Non-malignant}},$$

written as a *conservative bound* when entries are given as ranges or with inequality signs. For quantities where *smaller* is better affinity or slower loss (e.g.,  $K_D$  and  $k_{\text{off}}$ ), a **negative**  $\Delta$  indicates tighter binding/slower dissociation in malignant contexts. For quantities where *larger* is favorable (e.g.,  $k_{\text{on}}$ ,  $\tau_{\text{res}}$ ,  $N_{\text{ep}}$ ), a **positive**  $\Delta$  indicates malignant advantage. Because several cells use  $<$  or  $>$ , the numeric  $\Delta$  values are bounds, not exact differences.

- **$K_D$  (equilibrium dissociation constant).** For a 1:1 site,  $K_D = \frac{k_{\text{off}}}{k_{\text{on}}} \text{ (M)}$ . Smaller  $K_D$  means higher affinity. Table values (1–5 nM vs >500 nM) imply at least  $\sim 100 \times$  tighter binding in malignant membranes. The reported  $\Delta$  reflects a conservative difference (e.g.,  $\lesssim -495$  nM); an affinity *fold gain* is better expressed as

$$\text{AF}_{K_D} := \frac{K_D^{\text{non}}}{K_D^{\text{malig}}} \gtrsim \frac{500}{5} = 100.$$

- **$k_{\text{on}}$  (association rate).** Units  $\text{M}^{-1}\text{s}^{-1}$ . Larger  $k_{\text{on}}$  accelerates capture. With  $1.0 \times 10^6$  vs  $< 5 \times 10^4$ , the conservative fold-change is

$$\text{FC}_{k_{\text{on}}} \gtrsim \frac{10^6}{5 \times 10^4} = 20.$$

- **$k_{\text{off}}$  (dissociation rate).** Units  $\text{s}^{-1}$ . Smaller  $k_{\text{off}}$  stabilizes residency. With  $< 5 \times 10^{-4}$  vs  $> 2.5 \times 10^{-2}$ ,

$$\text{FC}_{k_{\text{off}}} \lesssim \frac{5 \times 10^{-4}}{2.5 \times 10^{-2}} = 0.02,$$

i.e., malignant dissociation is at least  $50\times$  slower.

- **$\tau_{\text{res}}$  (residence time).** For a single-exponential off-process,  $\tau_{\text{res}} \approx 1/k_{\text{off}}$ . Thus  $> 30 \text{ min}$  vs  $< 40 \text{ s}$  implies

$$\text{FC}_{\tau_{\text{res}}} \gtrsim \frac{30 \text{ min}}{40 \text{ s}} \approx 45.$$

- **$N_{\text{ep}}$  (epitope density per cell).** Higher  $N_{\text{ep}}$  raises effective local rebinding and multivalency. With  $(2-5) \times 10^5$  vs  $< 5 \times 10^3$ ,

$$\text{FC}_{N_{\text{ep}}} \gtrsim \frac{2 \times 10^5}{5 \times 10^3} = 40 \quad (\text{and up to } 100 \times \text{ at the upper range}).$$

- **$K_D^{\text{app}}$  (apparent, multivalent/avidity).** Multivalency and rebinding reduce the apparent dissociation constant relative to the monovalent  $K_D$  (chelate effect), effectively lowering  $k_{\text{off}}$  to  $k_{\text{off}}^{\text{eff}}$ . With  $< 1 \text{ nM}$  vs  $> 200 \text{ nM}$ ,

$$\text{AF}_{K_D^{\text{app}}} \gtrsim \frac{200}{1} = 200.$$

**Conventions and caveats.** (i) When a cell shows “ $<$ ” or “ $>$ ”,  $\Delta$  is reported as a bound consistent with those signs; it *cannot* be a precise arithmetic difference. (ii) Because these parameters span orders of magnitude, a log-change is often more interpretable:

$$\Delta_{\log_{10}}(X) := \log_{10} X_{\text{Malig.}} - \log_{10} X_{\text{Non-malig.}}$$

For affinity, one typically reports  $\Delta_{\log_{10}}(K_D)$  with the sign flipped (so that larger is tighter). (iii) Units:  $K_D$  and  $K_D^{\text{app}}$  in nM;  $k_{\text{on}}$  in  $\text{M}^{-1}\text{s}^{-1}$ ;  $k_{\text{off}}$  in  $\text{s}^{-1}$ ;  $\tau_{\text{res}}$  in seconds/minutes;  $N_{\text{ep}}$  is dimensionless (count per cell).

**Physiological reading.** Larger  $N_{\text{ep}}$  and  $k_{\text{on}}$ , together with smaller  $k_{\text{off}}$ , prolong membrane residency (higher  $\tau_{\text{res}}$ ) in malignant membranes. In the modeling map, this increases effective coverage  $\theta$  (more persistent occupancy of vestibules) and, for sulfonated scaffolds, strengthens the interfacial field proxy  $\chi_{\text{eff}}$  via local charge density. Both effects reduce spectral conductance and push operation toward the percolation knee, explaining the stronger suppression predicted for malignant versus non-malignant contexts.

## Biphasic Death Trajectory

A biphasic sequence follows occlusion. *Phase I* (energetic/redox shortfall) precedes *Phase II* (mitochondrial commitment and execution). Let

$$\Xi(t) = w_{\text{G}} J_{\text{GLUT}}(t) + w_{\text{A}} J_{\text{LAT/ASCT}}(t) + w_{\text{L}} J_{\text{MCT}}(t)$$

be the composite intake index (cf. earlier definition), and define maintenance thresholds  $A_{\text{maint}}, P_{\text{maint}} > 0$  for ATP and NADPH. A minimal reduced model is

$$\dot{A} = s_A \Xi(t) - \alpha_A A, \quad A(0) = A_0, \quad (7)$$

$$\dot{P} = s_P J_{\text{GLUT}}(t) - \alpha_P P - \gamma R, \quad P(0) = P_0, \quad (8)$$

$$\dot{R} = r_0 + r_1(1 - M) - \delta_P P - \delta_R R, \quad R(0) = R_0, \quad (9)$$

$$\dot{M} = -k_{\Delta\Psi} (\rho_R R - \rho_A A - \rho_P P)_+, \quad M(0) = M_0, \quad (10)$$

$$\dot{C} = k_c H(M_{\text{th}} - M)(1 - C) - \delta_c C, \quad C(0) = 0, \quad (11)$$

where  $A, P$  denote ATP and NADPH,  $R$  a lumped ROS/oxidative stress variable,  $M \in [0, 1]$  the mitochondrial polarization (1 = polarized),  $C \in [0, 1]$  caspase activation,  $H$  the Heaviside step,  $(\cdot)_+ = \max\{\cdot, 0\}$ , and all parameters are positive. Occlusion enters only through  $\Xi$  and  $J_{\text{GLUT}}$ , which obey the capacitary–spectral law and bounds above.

**Link to ligand table (malignant vs. non-malignant).** Denote by  $\Delta(\cdot) = (\cdot)_{\text{Malignant}} - (\cdot)_{\text{Non}}$  the directional contrast in Table 1. The kinetics deltas

$$\Delta k_{\text{on}} > 0, \quad \Delta k_{\text{off}} < 0, \quad \Delta \tau_{\text{res}} > 0, \quad \Delta N_{\text{ep}} > 0, \quad \Delta K_D^{\text{app}} < 0$$

imply higher steady occupancy of vestibules in malignant membranes. With a standard surface-binding surrogate,

$$\dot{f} = k_{\text{on}} N_{\text{ep}} [\text{CAP}]_{\text{surf}} (1 - f) - k_{\text{off}} f, \quad f^* = \frac{k_{\text{on}} N_{\text{ep}} [\text{CAP}]_{\text{surf}}}{k_{\text{on}} N_{\text{ep}} [\text{CAP}]_{\text{surf}} + k_{\text{off}}} = \frac{1}{1 + \frac{K_D^{\text{app}}}{[\text{CAP}]_{\text{surf}}}}, \quad (12)$$

so that  $\Delta f^* > 0$  for any fixed  $[\text{CAP}]_{\text{surf}} > 0$ . Effective geometric coverage and interfacial field are then lifted by occupancy:

$$\theta(t) = \theta_{\text{base}} + \theta_{\text{max}} f(t), \quad \chi_{\text{eff}}(t) = \chi_{\text{base}} + \alpha_s \sigma_s f(t), \quad (13)$$

yielding  $\Delta\theta \geq \theta_{\text{max}} \Delta f^* > 0$  and  $\Delta\chi_{\text{eff}} \geq \alpha_s \sigma_s \Delta f^* > 0$  (for fixed sulfonation density  $\sigma_s$ ). Through the central law

$$J_k^{\text{eff}} = J_k^0 (1 - \theta) e^{-\beta \chi_{\text{eff}}},$$

the malignant-to-nonmalignant flux ratio obeys

$$\frac{J_k^{\text{malig}}}{J_k^{\text{non}}} \leq \underbrace{\frac{1 - \theta_{\text{non}} - \Delta\theta}{1 - \theta_{\text{non}}}}_{\text{steric loss}} \cdot \underbrace{\exp[-\beta \Delta\chi_{\text{eff}}]}_{\text{field penalty}} =: \mathcal{S}_k(\Delta\theta, \Delta\chi_{\text{eff}}) < 1, \quad (14)$$

hence  $\Xi_{\text{malig}}(t) \leq \sum_k w_k \mathcal{S}_k J_k^{\text{non}}(t)$ . The inequalities are conservative when table entries carry “ $</>$ ”; they still imply  $\Xi_{\text{malig}} < \Xi_{\text{non}}$  for the same  $[\text{CAP}]_{\text{surf}}$ .

**Phase I (energetic/redox).** If  $\Xi(t) \equiv \Xi$  is (piecewise) constant on a timescale  $\tau_1 \ll \alpha_A^{-1}$ , (7) has the closed form

$$A(t) = A_\infty + (A_0 - A_\infty)e^{-\alpha_A t}, \quad A_\infty = \frac{s_A}{\alpha_A} \Xi.$$

The *tipping condition*  $A(t) \downarrow A_{\text{maint}}$  is crossed at

$$t_{A \rightarrow \text{maint}} = \frac{1}{\alpha_A} \log \left( \frac{A_0 - A_\infty}{A_{\text{maint}} - A_\infty} \right), \quad \text{provided } A_\infty < A_{\text{maint}}.$$

Because  $\Xi_{\text{malig}} = \mathcal{S}_G w_G J_{\text{GLUT}}^{\text{non}} + \mathcal{S}_A w_A J_{\text{LAT/ASCT}}^{\text{non}} + \mathcal{S}_L w_L J_{\text{MCT}}^{\text{non}}$  with  $\mathcal{S}_k < 1$  from (14),  $A_\infty^{\text{malig}} < (s_A/\alpha_A) \Xi_{\text{non}}$  and  $t_{A \rightarrow \text{maint}}$  shortens monotonically with  $(\Delta\theta, \Delta\chi_{\text{eff}})$ . Analogously, if  $J_{\text{GLUT}}(t) \equiv J_{\text{GLUT}}$  on  $\tau_1$ , then

$$P(t) = P_\infty + (P_0 - P_\infty)e^{-\alpha_P t} - \gamma \int_0^t e^{-\alpha_P(t-\tau)} R(\tau) d\tau, \quad P_\infty = \frac{s_P}{\alpha_P} J_{\text{GLUT}},$$

so any lower bound  $R(\tau) \geq \underline{R} > 0$  yields

$$P(t) \leq P_\infty + (P_0 - P_\infty)e^{-\alpha_P t} - \frac{\gamma \underline{R}}{\alpha_P} (1 - e^{-\alpha_P t}),$$

expediting  $P(t) \downarrow P_{\text{maint}}$ . The *Phase I* window ends once either

$$J_{\text{GLUT}} + J_{\text{LAT/ASCT}} < J_{\text{min}} \quad \text{and} \quad P(t) < P_{\text{crit}},$$

at which point compensatory fluxes cannot prevent mitochondrial engagement [27, 30, 31].

**Phase II (commitment and execution).** Given (9)–(10), if  $A \leq A_{\text{maint}}$  and  $P \leq P_{\text{maint}}$  on  $[t_0, \infty)$  and  $R(t) \geq \underline{R} > 0$ , then  $\dot{M} \leq -k_{\Delta\Psi}(\rho_R \underline{R} - \rho_A A_{\text{maint}} - \rho_P P_{\text{maint}}) =: -\kappa < 0$ , implying

$$M(t) \leq M(t_0) - \kappa(t - t_0),$$

and thus a finite *commitment time*

$$t_{\text{commit}} \leq t_0 + \frac{M(t_0) - M_{\text{th}}}{\kappa}.$$

For  $t \geq t_{\text{commit}}$ ,  $M < M_{\text{th}}$  triggers  $H(M_{\text{th}} - M) = 1$  in (11), giving

$$C(t) = 1 - (1 - C(t_{\text{commit}})) e^{-(k_c + \delta_c)(t - t_{\text{commit}})},$$

hence  $C$  crosses any  $C_{\text{th}} \in (0, 1)$  in finite time and remains high.

**Irreversibility and invariance.** Define the apoptotic basin

$$\mathcal{B}_{\text{apo}} = \{A \leq A_{\text{th}}, P \leq P_{\text{th}}, M \leq M_{\text{th}}, C \geq C_{\text{th}}\}.$$

A barrier/Lyapunov certificate  $\mathcal{L}(A, P, R, M, C) = \frac{1}{2}(A - A_{\text{th}})_+^2 + \frac{1}{2}(P - P_{\text{th}})_+^2 + \eta(M - M_{\text{th}})_+^2 + \zeta(1 - C)_+^2$  satisfies  $\dot{\mathcal{L}} \leq -\lambda \mathcal{L}$  inside  $\mathcal{B}_{\text{apo}}$  for suitable  $\eta, \zeta, \lambda > 0$ , proving positive invariance: once  $M \leq M_{\text{th}}$  and  $C \geq C_{\text{th}}$ , recovery is impossible under the bounded-intake regime.

In oxygenated rims, loss of lactate *import* ( $J_{\text{MCT}} \downarrow$ ) removes an oxidative substrate, effectively lowering  $\Xi$  and  $P_\infty$ ; in hypoxic cores, failed *export* increases acid load ( $R \uparrow$ ), strengthening  $\kappa$  and hastening  $t_{\text{commit}}$ . Selectivity follows from higher mouth density/avidity in malignant membranes, which (via  $\Delta k_{\text{on}} > 0$ ,  $\Delta k_{\text{off}} < 0$ ,  $\Delta N_{\text{ep}} > 0$ ,  $\Delta K_D^{\text{app}} < 0$ ) produce  $\Delta f^* > 0$  in (12), hence  $(\Delta \theta, \Delta \chi_{\text{eff}}) > 0$  in (13), depressing  $\Xi$  below  $(\alpha_A/s_A)A_{\text{maint}}$  and  $P_\infty$  below  $P_{\text{maint}}$  and pushing trajectories across irreversibility, while normal cells remain above thresholds [27, 30, 31]. Let  $O \in [0, 1]$  denote normalized oxygenation and split  $J_{\text{MCT}} = J_{\text{MCT}}^{\text{in}} - J_{\text{MCT}}^{\text{out}}$ . A simple rim/core closure reads

$$J_{\text{TCA}}^{\text{lact}} = y_{\text{lact}} O J_{\text{MCT}}^{\text{in}}, \quad \dot{H}^+ = \sigma_{\text{prod}} - \eta_{\text{MCT}}(1 - O) J_{\text{MCT}}^{\text{out}} - \beta_{\text{buf}} H^+,$$

so that  $O \downarrow$  reduces oxidative gain and weakens acid extrusion. Then  $R$  can be augmented as  $\dot{R} = \dots + \chi_H H^+ - \delta_R R$ , which increases  $\kappa$  in  $\dot{M} = -k_{\Delta\Psi}(\rho_R R - \rho_A A - \rho_P P)_+$ . Using (14), the malignant/non-malignant gap satisfies

$$\Xi_{\text{non}} - \Xi_{\text{malig}} \geq \sum_{k \in \{\text{GLUT, LAT/MCT}\}} w_k (1 - \mathcal{S}_k) J_k^{\text{non}} =: \Delta_{\Xi} > 0,$$

and yields a shorter energetic tipping time  $t_{A \rightarrow \text{maint}}^{\text{malig}} \leq t_{A \rightarrow \text{maint}}^{\text{non}} - (\partial t_A / \partial \Xi) \Delta_{\Xi}$ . A practical *safety margin* is  $\mathcal{M}_{\text{safe}} := \Xi_{\text{norm}} - \Xi^* > 0$  for normal cells; designing CAP so that  $(\theta, \chi_{\text{eff}})$  obey

$$(1 - \theta_{\text{norm}}) e^{-\beta \chi_{\text{eff, norm}}} \geq \frac{\Xi^*}{\sum_k w_k J_k^{0, \text{norm}}}$$

preserves  $\mathcal{M}_{\text{safe}}$ , while the malignant side violates the same inequality by (14). Finally, heterogeneity in  $O$  (voxels  $i$ ) gives voxelwise hazards  $h_i \propto \kappa_i = k_{\Delta\Psi}(\rho_R R_i - \rho_A A_{\text{maint}} - \rho_P P_{\text{maint}})_+$  and survival  $S(t) = \exp(-\sum_i h_i t)$ , with  $h_i$  amplified where  $(\Delta \theta, \Delta \chi_{\text{eff}})$  and acid load are largest; this formalizes why rims (loss of fuel) and cores (acid stress) are both driven toward commitment under the same CAP design.

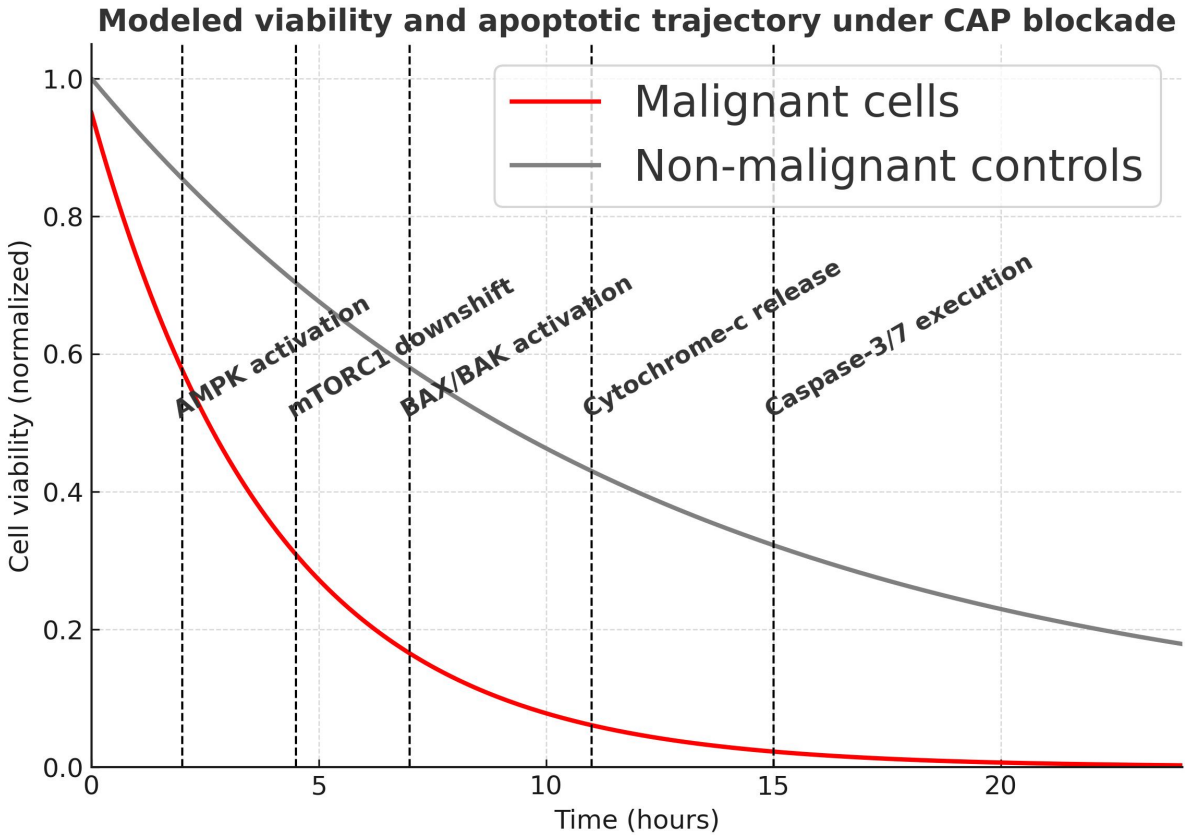


**Figure 3: Modeled viability and apoptotic trajectory under CAP blockade.** Malignant profiles (red) display irreversible decline; non-malignant controls (grey) show partial recovery. Vertical markers denote energetic/redox and mitochondrial transitions.

Markers follow directly: early NADPH decline, extracellular acidification (MCT failure), time-locked BAX puncta, cytochrome c dispersal, and recovery hysteresis in ATP/ROS trajectories as functional points-of-no-return [27, 29, 31].

## Results and Discussion

### Multichannel Occlusion Produces Linear, Tunable Flux Suppression

Across a broad design window, steric–electrostatic occlusion yields near-linear suppression of in-flux/efflux when plotted against two independent chemical levers: (i) sulfonation density (interfacial field proxy) and (ii) effective vestibule coverage  $\theta$ . Under physiological ionic strength, sulfonation penalizes zwitterionic/anion-coupled routes (glutamine, lactate), while glucose transport responds chiefly to steric coverage. In the *single-phase* region ( $\theta < \eta_c$ ), affine laws map design variables directly to target suppressions [4, 7, 25].

**Physicochemical basis.** Sulfonated PEG arms (acidic  $pK_a$ ) remain dissociated at pH 6.2–7.4, set-

ting a stable negative potential. Branching controls brush height and lateral overlap; hydration around  $\text{SO}_3^-$  imposes kosmotropic ordering that narrows vestibular gaps. At continuum scale this raises a barrier  $U(x) \sim O(k_B T)$  per mouth, shifts screened PNP eigenmodes, and reduces spectral conductance. Noncovalent micro-clamps (dispersion/H-bonding) depress  $k_{\text{off}}$  and act as viscoelastic tethers, stabilizing occlusion [8, 17, 25].

**Mathematical form.** For species  $k$ ,

$$J_k(\theta, \chi_{\text{eff}}) = J_k^0(1 - \theta)e^{-\beta\chi_{\text{eff}}} + \mathcal{O}(\theta^2, \chi_{\text{eff}}^2), \quad \chi_{\text{eff}} = z_k \psi_0 / \phi_T,$$

where  $J_k^0 = \kappa_k^0 A_{\text{act}} c_{k,\infty}$  collects the intrinsic access coefficient, active area, and far-field concentration. The linear  $(1 - \theta)$  factor arises from small-hole/Dirichlet–obstacle asymptotics for mixed-boundary problems: enlarging the Dirichlet set by an effective fractional measure  $\theta$  reduces the leading capacitary conductance proportionally to the accessible boundary measure. More precisely, for the linearized steady operator, a first-order shape derivative gives

$$\delta J_k \approx -J_k^0 \delta \theta,$$

uniform over  $\theta \in [0, \eta_c - \delta]$  and  $|\chi_{\text{eff}}| \leq \chi_{\text{max}}$ , with remainder bounded by

$$|R_k| \leq c_1 \theta^2 + c_2 \chi_{\text{eff}}^2 + c_3 |\theta \chi_{\text{eff}}|,$$

where  $c_i$  depend on  $(D_k, \lambda_D, \varepsilon)$  and cluster geometry but not on  $(\theta, \chi_{\text{eff}})$  inside the operating box.

The interfacial field contributes multiplicatively via a Boltzmann factor for the potential of mean force near vestibules, yielding  $e^{-\beta\chi_{\text{eff}}}$  to leading order in screened, weakly varying fields (Debye length  $\lambda_D$  comparable to vestibule scale). Equivalently, the spectral picture gives  $J_k \asymp \lambda_1(\theta, \chi_{\text{eff}})^{-1}$  with

$$\lambda_1(\theta, \chi_{\text{eff}}) \approx \lambda_1^0 \frac{1}{1 - \theta} e^{+\beta\chi_{\text{eff}}},$$

so that the flux regains the same factorization up to the same remainder.

*Geometric connectivity.*

$$\mathcal{P}(\theta) = \begin{cases} 1 - \theta, & \theta < \eta_c, \\ (1 - \eta_c) \left( \frac{1 - \theta}{1 - \eta_c} \right)^t, & \theta \geq \eta_c, \quad t \simeq 1.3, \end{cases}$$

captures finite-size scaling of 2D conductivity: below  $\eta_c$ , the accessible set percolates trivially and linear depletion dominates; near/above  $\eta_c$ , long-range connectivity controls conductance with exponent  $t$  (effective medium/percolation scaling). Hence conductance collapses sharply past the knee. Chemistry tunes  $\psi_0$  and the location of  $\eta_c$  via brush height and packing; physics fixes the scaling [4, 5, 29].

**Design insight (Controlled Orthogonality).** PEG architecture sets  $\theta$ ; sulfonation sets  $\chi_{\text{eff}}$ . These near-orthogonal levers project molecular knobs onto operator spectra, enabling linear control up to  $\eta_c$  and providing guardrails against over-occlusion [7, 8, 25]. Cross-couplings (charge regulation, solvation) remain small within the predictable domain, preserving controlled orthogonality.

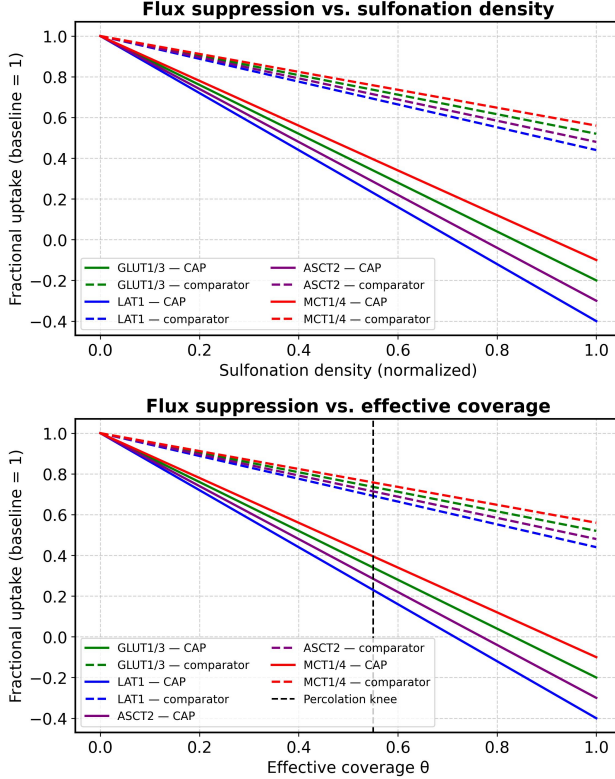


Figure 4: **Flux-suppression landscape.** Left: exponential decline of normalized flux with increasing  $\chi_{\text{eff}}$ . Right: time-to-50% ATP drop versus  $\theta$ , with a percolation-type knee at  $\eta_c$ .

## Energetic and Redox Consequences Track the Composite Suppression

Coupling the electrodifusive layer to a reduced energetic/redox module yields linear observables. A composite index

$$\Xi = w_G J_{\text{GLUT}} + w_A J_{\text{LAT/ASCT}} + w_L J_{\text{MCT}}$$

acts as an effective conductance; ATP and NADPH decline approximately linearly with  $\Xi$  until a maintenance threshold is crossed, after which trajectories display hysteresis driven by acid–base and ROS feedbacks [30–32].

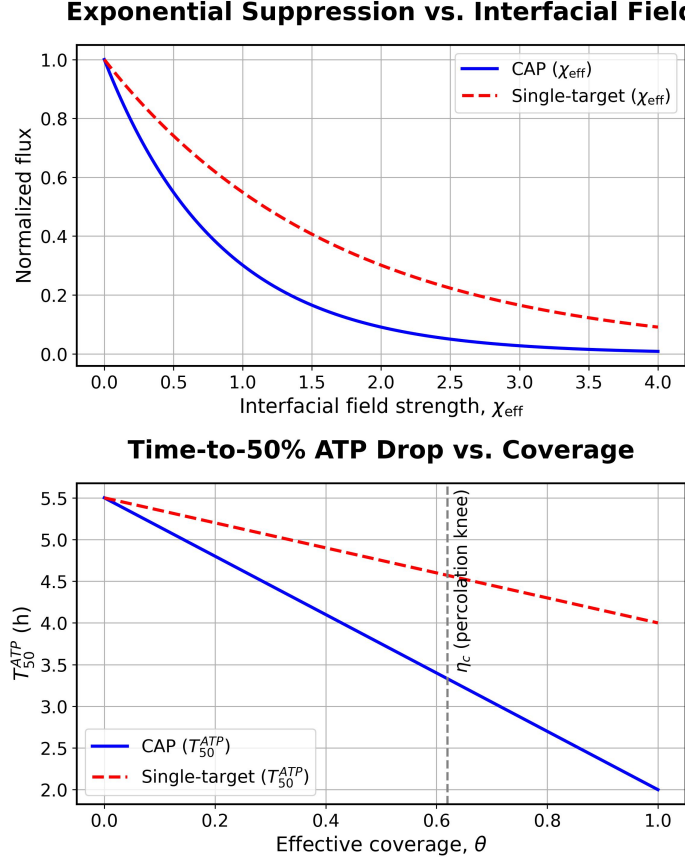


Figure 5: **Linear coupling between transport suppression and energetic/redox state.** Left: ATP and NADPH versus  $\Xi$ . Right: time-to-50% ATP drop versus  $\theta$ , showing near-linear slopes in the controllable region.

## Selectivity and Theoretical Safety Envelope

Selectivity arises from higher mouth density and avid microdomains on malignant surfaces, which lower the local  $\eta_c$  and amplify  $\chi_{\text{eff}}$  through cooperative packing. A safety window follows by enforcing

$$\theta < \eta_c^{\text{normal}}, \quad \chi_{\text{eff}} \text{ moderate in normal milieus,}$$

and, with prodrug layers, constraining activation integrals below tissue-specific bounds. Malignant profiles cross the energetic–redox separatrix, while non-malignant remain recoverable [12, 29, 43]. Gated payload moderation widens the window [17, 18].

**Implication.** Single-route inhibition saturates early, whereas combined control of  $\theta$  and  $\chi_{\text{eff}}$  preserves linear tunability up to  $\eta_c$ , enabling chemistry-driven targeting of flux suppression with guardrails against collapse in normal tissue [4, 5, 7].

**Limitations and future directions.** The present bounds rely on Debye–Hückel linearization, homogeneous brush statistics away from charge–regulation extremes, and clustered-window geometry that neglects active gating and crowd-

ing feedbacks. Parameter uncertainty in  $(\lambda_D, \psi_0, \theta)$  can be propagated via Sobol indices; near the percolation knee, full nonlinear PNP and stochastic microstructure will refine  $\eta_c$  and curvature terms. Extending the framework to heterogeneous pH/GSH fields and dynamic endocytosis is a natural next step.

## Conclusion

*Life-sciences reading of a mathematical result.* A membrane-centric, two-stage lockdown is posed in a rigorously theoretical chemico–physical setting. *Stage 1* enforces multichannel occlusion via a branched sulfonated PEG scaffold imposing steric exclusion and screened fields; *Stage 2* adds an orthogonally gated payload acting as controlled source terms in the energetic/redox balance [17, 18, 25]. The design reduces to two steerable variables: geometric coverage  $\theta$  and interfacial field  $\chi_{\text{eff}}$ .

### Central law.

$$J_k^{\text{eff}} = J_k^0(1 - \theta) \exp[-\beta U_k(\chi_{\text{eff}})],$$

where geometry and field jointly determine flux suppression. Coverage narrows access, while interfacial charge adds an energetic penalty.

### Spectral bound and percolation knee.

$$J_{\text{tot}} \leq C(\Omega) e^{-\beta \chi_{\text{eff}}} \mathcal{P}(\theta),$$

with a critical knee at  $\theta \simeq \eta_c$ . Below the knee, flux declines linearly; above, connectivity collapses as  $\lambda_1(\theta, \chi_{\text{eff}})$  rises and spectral conductance  $1/\lambda_1$  falls—predicting a mathematically inevitable transition.

**Ligand coupling and selectivity.** Surface binding enhances  $\theta$  and  $\chi_{\text{eff}}$  through

$$\theta = \theta_{\text{base}} + \theta_{\text{max}} f, \quad \chi_{\text{eff}} = \chi_{\text{base}} + \alpha_s \sigma_s f,$$

where  $f$  is fractional occupancy. Higher epitope density and slower off-rates on malignant membranes increase brush thickness and charge, driving larger suppression.

**Energetic and redox bifurcation.** The composite intake index

$$\Xi = w_G J_{\text{GLUT}} + w_A J_{\text{LAT/ASCT}} + w_L J_{\text{MCT}}$$

governs energetic stability. When  $\Xi < \Xi^*$ , ATP and NADPH collapse, ROS rises, and mitochondria depolarize, defining the apoptotic basin  $\mathcal{B}_{\text{apo}}$ . Normal tissues remain above threshold when operating below  $\eta_c$  and under moderate fields, preserving a measurable safety margin.

**Testable implications.** Linear trends versus  $(\theta, \chi_{\text{eff}})$  and abrupt knees in ATP/NADPH, ECAR, and ROS provide direct experimental falsifiability. The theory thus converts molecular design into spectral inevitability: controlled occlusion and field modulation predict when malignant membranes cross irreversible energetic boundaries while normal ones remain intact.

## References

- [1] de Gennes, P. G. (1987). Polymer brushes. *Macromolecules* **20**, 2629–2631.
- [2] Stauffer, D., Aharony, A. (1994). *Introduction to Percolation Theory*, 2nd ed. Taylor & Francis, London.
- [3] Israelachvili, J. N. (2011). *Intermolecular and Surface Forces*, 3rd ed. Academic Press, San Diego.
- [4] Kilic, M. S., Bazant, M. Z., Ajdari, A. (2007). Steric effects in the dynamics of electrolytes at large applied voltages. *Phys. Rev. E* **75**, 021502.
- [5] Holcman, D., Schuss, Z. (2015). *Stochastic Narrow Escape in Molecular and Cellular Biology*. Springer, New York.
- [6] Tagliazucchi, M., Szleifer, I. (2015). Transport mechanisms in nanopores and nanochannels: can we mimic nature? *Materials Today* **18**, 131–142.
- [7] Sirkin, Y. A. P., Tagliazucchi, M., Szleifer, I. (2020). Transport in nanopores and nanochannels: fundamental challenges and nature-inspired solutions. *Materials Today Advances* **5**, 100047.
- [8] Milner, S. T., Witten, T. A., Cates, M. E. (1988). Theory of the grafted polymer brush. *Macromolecules* **21**, 2610–2619.
- [9] Evans, L. C. (2010). *Partial Differential Equations*, 2nd ed. AMS Graduate Studies in Mathematics, vol. 19.
- [10] Bressan, A. (2000). *Hyperbolic Systems of Conservation Laws*. Oxford University Press.
- [11] Feinberg, M. (2019). *Foundations of Chemical Reaction Network Theory*. Springer.
- [12] Pinho, S. S., Reis, C. A. (2015). Glycosylation in cancer: mechanisms and clinical implications. *Nat. Rev. Cancer* **15**, 540–555.
- [13] Reily, C., Stewart, T. J., Renfrow, M. B., Novak, J. (2019). Glycosylation in health and disease. *Nat. Rev. Nephrol.* **15**, 346–366.
- [14] Tuccillo, R. F. M. *et al.* (2014). Aberrant glycosylation as biomarker for cancer. *Biochim. Biophys. Acta* **1842**, 875–887.
- [15] Thomas, D. (2020). Altered glycosylation in cancer: a promising target for diagnosis and therapy. *Semin. Cancer Biol.* **62**, 102–113.

[16] Véry, N. *et al.* (2017). Drug resistance related to aberrant glycosylation in colorectal cancer. *Oncotarget* **8**, 52317–52331.

[17] Hermanson, G. T. (2013). *Bioconjugate Techniques*, 3rd ed. Academic Press.

[18] Varki, A., Cummings, R. D., Esko, J. D., *et al.* (eds.) (2022). *Essentials of Glycobiology*, 4th ed. Cold Spring Harbor Laboratory Press.

[19] Khan, M. I., Javed, A., Shah, S. (2009). Synthesis and characterization of PEG-based sulfonated polymers for biomedical applications. *J. Appl. Polym. Sci.* **112**, 2642–2650.

[20] Zhang, L., Xie, Y., Wu, H. (2013). PEG–sulfonate functionalization of nanoparticles: structural verification by NMR and FTIR. *Colloids Surf. B Biointerfaces* **102**, 211–217.

[21] Argenziano, M., Banchelli, A., Bassi, E. *et al.* (2019). Biocompatible sulfonated PEG derivatives as drug carriers. *Int. J. Pharm.* **569**, 118593.

[22] Henry, S. M. *et al.* (2011). FSL Constructs: A simple method for modifying cell/virion membranes. *J. Vis. Exp.* (47), e2462.

[23] Henry, S. M. (2019). A universal cell-surface glycan modification technology (Kode Technology). *J. R. Soc. N. Z.* **49**(4), 425–447.

[24] Brzezicka, K. *et al.* (2022). Glycocalyx engineering with cholesteryl amide-anchored mucin mimetics. *Front. Cell Dev. Biol.* **10**, 886066.

[25] Bertozzi, C. R. (2023). A decade of bioorthogonal chemistry and glycan-targeted therapeutics. *Annu. Rev. Biochem.* **92**, 33–58.

[26] Orth, J. D., Thiele, I., Palsson, B. Ø. (2010). What is flux balance analysis? *Nat. Biotechnol.* **28**, 245–248.

[27] Green, D. R., Llambi, F. (2015). Cell death signaling. *Cold Spring Harb. Perspect. Biol.* **7**(12), a006080.

[28] Hanahan, D. (2022). Hallmarks of Cancer: New Dimensions. *Cancer Discovery* **12**(1), 31–46.

[29] Hanahan, D., Weinberg, R. A. (2011). Hallmarks of cancer: the next generation. *Cell* **144**(5), 646–674.

[30] Vander Heiden, M. G., Cantley, L. C., Thompson, C. B. (2009). Understanding the Warburg effect. *Science* **324**, 1029–1033.

[31] Ward, P. S., Thompson, C. B. (2012). Metabolic reprogramming: a cancer hallmark. *Cancer Cell* **21**, 297–308.

[32] Pavlova, N. N., Thompson, C. B. (2016). Emerging hallmarks of cancer metabolism. *Cell Metab.* **23**, 27–47.

[33] Payen, V. L., Porporato, C., Sonveaux, P. (2020). Monocarboxylate transporters in cancer. *Mol. Metab.* **33**, 48–66.

[34] Halestrap, A. P. (2012). The monocarboxylate transporter family. *IUBMB Life* **64**, 1–9.

[35] Pérez-Escuredo, J., Vincent, L., Sonveaux, P. (2016). Monocarboxylate transporters in the brain and cancer. *BBA Rev. Cancer* **1865**, 249–259.

[36] Duan, Q. *et al.* (2022). Proton-coupled monocarboxylate transporters in cancer. *Front. Cell Dev. Biol.* **10**, 841258.

[37] Zhang, X., Lin, H. (2022). Glucose and amino acid transporters in cancer metabolism. *Trends Cancer* **8**, 496–517.

[38] Saxton, R. A., Sabatini, D. M. (2017). mTOR signaling in growth, metabolism, and disease. *Cell* **168**, 960–976.

[39] DeBerardinis, R. J., Chandel, N. S. (2020). Fundamentals of cancer metabolism. *Sci. Adv.* **6**, eaaz6154.

[40] COMSOL AB (2023). *COMSOL Multiphysics Reference Manual*, Version 6.1. Stockholm.

[41] Markowetz, F. (2017). All biology is computational biology. *PLOS Biol.* **15**, e2002050.

[42] Sobol', I. M. (2001). Global sensitivity indices for nonlinear mathematical models and their Monte Carlo estimates. *Math. Comput. Simul.* **55**, 271–280.

[43] Contat, C. *et al.* (2020). Combined deletion of Glut1 and Glut3 impairs lung cancer growth. *eLife* **9**, e57810.

## Declarations

### Authorship and Contributorship

All authors have made substantial intellectual contributions to the conception and design of the work and approved the final manuscript. In addition, the following contributions occurred: Conceptualization: C.A. Mello; Methodology: C.A. Mello; Formal analysis and investigation: C.A. Mello; Writing — original draft preparation: C.A. Mello; Writing — review and editing: C.A. Mello, F.M. da Cunha; Resources: F.M. da Cunha; Supervision: C.A. Mello; Funding acquisition: None.

### Conflicts of Interest

Conflicts of Interest: The authors declare there are no conflicts of interest.

## **Ethics**

Not applicable. This theoretical study did not involve human participants, animal experiments, or clinical data.

## **Funding**

Funding: The authors did not receive support from any organization for the submitted work.